



Asymmetric Cosine Jerk Trajectory Optimization for Robust Vibration Suppression

Yi Fang , Ruoyi Hao , Graduate Student Member, IEEE, Hao Fan , Yu Tian , and Hongliang Ren , Senior Member, IEEE

Abstract—Rapid and precise movements of industrial equipment necessitate reference trajectory design to mitigate motion-induced vibrations, which becomes more challenging in the presence of system uncertainties. This article develops a novel trajectory planning method based on an improved cosine jerk model to robustly suppress residual vibration under actuator limits. Incorporating tunable asymmetry into the model allows trajectories to start faster and shorten motion duration. By applying a linear transformation in the complex domain, the vibration suppression capability is extended to accommodate both undamped and damped systems. The profile parameters are modulated to align the intrinsic trajectory zeros with the system poles, attenuating spectral components near the critical modal frequency that excite resonance. Unlike much current work that provides only partial solutions or requires numerical optimization, a complete analytical solution is derived for all possible trajectory types using a designed coefficient that manages the acceleration ratio. The effectiveness and robustness of the method are validated experimentally across different systems. The results show that the proposed method can achieve better vibration mitigation performance under modeling errors than existing benchmark methods.

Index Terms—Asymmetric trajectory, motion profile, residual vibration, robustness, trajectory planning.

Received 30 August 2025; accepted 11 October 2025. This work was supported in part by Hong Kong Research Grants Council Collaborative Research Fund under Grant CRF C4026-21GF; in part by the General Research Fund under Grant GRF 14216022, Grant 14204524, and Grant GRF 14203323; in part by the National Natural Science Foundation of China under Grant 52105031; and in part by Guangdong Basic and Applied Basic Research Foundation under Grant 2021B1515120035. (Corresponding author: Hongliang Ren.)

Yi Fang is with the School of Automation and Intelligent Sensing, Shanghai Jiao Tong University, Shanghai 200240, China, and also with the Department of Electronic Engineering, The Chinese University of Hong Kong, Hong Kong (e-mail: apocalypse@sjtu.edu.cn).

Ruoyi Hao and Yu Tian are with the Department of Electronic Engineering, The Chinese University of Hong Kong, Hong Kong (e-mail: 1155167067@link.cuhk.edu.hk; 1155187967@link.cuhk.edu.hk).

Hao Fan is with the School of Automation and Intelligent Sensing, Shanghai Jiao Tong University, Shanghai 200240, China (e-mail: fanhao1026@sjtu.edu.cn).

Hongliang Ren is with the Department of Electronic Engineering, The Chinese University of Hong Kong, Hong Kong and also with Shenzhen Loop Area Institute, Shenzhen 518045, China (e-mail: hlren@ieee.org).

Digital Object Identifier 10.1109/TIE.2025.3625296

I. INTRODUCTION

AUTOMATIC machines such as positioning stages, robot manipulators, machine tools, and cranes are widely used in modern industry to provide higher productivity, precision, and reliability. Designing fast and accurate reference motion profiles is a key research issue involving conflicting objectives. Motion-induced vibrations in high-speed operations pose a critical challenge across engineering fields, deteriorating efficiency and performance, and potentially compromising both mechanical components and payload safety. For instance, flexible or suspended objects handled by robot arms may vibrate at their target positions, necessitating extra time for stabilization before subsequent operations [1]. In precision machining, unwanted vibrations can cause contouring errors and destroy surface integrity [2]. Similarly, semiconductor manufacturing requires vibration-free wafer transfer and lithography scanning processes [3].

Currently, the trapezoidal velocity profile is the most prevalent method in practice for its speed and simplicity, but acceleration discontinuities lead to jerk spikes that excite resonances, causing severe vibration and longer settling. This motivates researchers to focus on trajectory optimization to attenuate undesirable critical frequency components in the reference trajectory. Input shaping is a popular feedforward solution that convolves the original command with impulse sequences designed based on the modal parameters. First formalized by [4], robust variants such as zero vibration derivative (ZVD) and extra-insensitive (EI) have been successfully implemented across various machines [5]. Nevertheless, input shaping distorts reference trajectories, creating multiple acceleration jumps that necessitate high-bandwidth servo drives for accurate tracking [6]. Another well-known technique is trajectory smoothing, which aims to meticulously design profiles with a high degree of continuity. One representative method is the S-curve profile [7], [8], which constrains the rising and falling times of acceleration with controlled jerks. Limited-jerk trajectories have proven superior in reducing actuator strain, enhancing tracking performance, and extending machine lifespan [9], making them particularly suitable for precision tasks. Moreover, they are essential for alleviating psychological stress during close-proximity human–robot interactions [10].

In the past decade, the planning of higher-order polynomial S-curve trajectories subject to derivative bound constraints

has attracted increasing investigation using various methods, including filtering techniques [11], integrator chains [12], algebraic computations [13], and recursive methods. As indicated in [14], higher-order trajectories yield better performance due to their inherently lower harmonic content at high frequencies. Unfortunately, the parameter computation process becomes rather cumbersome as the trajectory order increases because of more involved segments. Most of these methods overlook dynamic characteristics of systems, such as modal frequency and damping, which are tightly coupled with vibratory behavior. The latest findings suggest that the period of jerk impulses must be appropriately selected based on the natural period to minimize residual vibrations [3], [15].

The application of trigonometric functions has also emerged as a sophisticated option for establishing smooth trajectory models [16], [17], [18]. Prior research has empirically shown that trigonometric S-curves outperform the standard polynomial S-curve with constant jerk in terms of positioning accuracy and robustness [19], [20]. A trade-off for smoother profiles is increased execution time for a given set of actuator limits. For this reason, asymmetric motion profiles have attracted growing interest [21], [22], [23], [24]. Allowing a fast beginning during the acceleration phase and a slow yet smooth finish during the deceleration phase enables superior outcomes in both vibration level and trajectory duration. A main challenge in using asymmetric trajectories is the complex derivation process for additional parameters. The published literature often provides only partial solutions that are feasible under limited constraint conditions [25]. Although [26] derived a closed-form solution using a jerk scaling parameter, frequency constraints are neglected and the coupling among motion segments restricts the model generality. To minimize residual vibration, early studies relied on heuristic trial-and-error tuning [27]. More recently, several articles have attempted to optimize motion parameters by analyzing vibration responses in the time and Laplace domains [28], [29], [30]. However, these works are based on constant jerk models, and their effectiveness deteriorates when modal damping becomes nonnegligible.

Based on the above analysis, existing smooth trajectory planning methods that consider both kinematic and frequency constraints often lack a complete solution or degrade under high damping and modeling errors, limiting their applicability in certain scenarios. In light of this, this article presents a novel asymmetric trajectory optimization method for motion-induced residual vibration reduction based on a trigonometric jerk model, as illustrated in Fig. 1. This approach is suitable for a wide variety of applications, as it applies to any system characterized by a linear or linearized dynamic model. The primary objective is to mitigate the adverse effects of the dominant flexible mode on positioning while minimizing trajectory duration, especially in highly damped systems. The optimized trajectory synthesizes the inherent smoothness of S-curve profiles with the targeted frequency cancellation of input shaping. This work does not aim to design dedicated controllers tailored for specific plants. Instead, the proposed method operates at the motion planning level and is easy to implement on general devices that use closed and proprietary controllers. It provides a practical

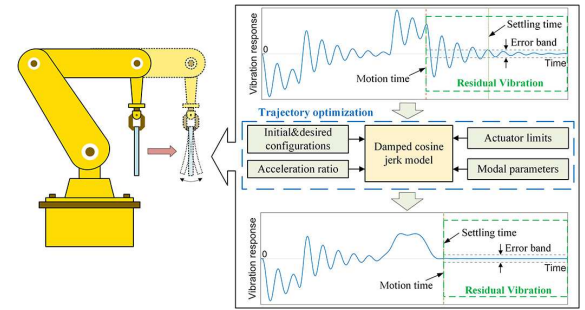


Fig. 1. Trajectory optimization for canceling the dominant mode. The asymmetric damped cosine jerk trajectory incorporates both modal frequency and damping ratio to eliminate residual vibration while minimizing settling time.

tool without requiring any hardware modifications. Although the design of control systems is not the main objective, an effective control system can ensure accurate trajectory tracking. This aspect will also be discussed in the experimental section.

The main contributions of this article are outlined as follows.

- 1) An asymmetric damped cosine jerk-based model that ensures continuity up to the snap level is designed to enable more efficient motion and facilitate parameter adjustment. This trajectory model extends the robust vibration suppression capability of the cosine jerk profile under system uncertainties to damped cases and potentially shortens the motion duration under high damping.

- 2) By introducing a proportional factor to manage the acceleration phase, all possible types of the trajectory model are characterized, allowing greater flexibility in tuning asymmetry. The established parameter optimization procedure provides a complete closed-form solution for arbitrary constraints without requiring numerical iterations, offering ease of practical implementation.
- 3) The proposed approach is experimentally validated on multiple platforms, demonstrating superior robustness in reducing vibration amplitude and settling time in the presence of modeling errors. Additionally, a control system for accurate trajectory tracking is developed.

The rest of this article is organized as follows. Section II reviews the characteristics of the cosine jerk profile. The developed asymmetric damped cosine jerk model and its formulations are presented in Section III. In Section IV, the parameter tuning rules for potential trajectory types are derived by analyzing critical constraint conditions. Section V provides the robustness analysis against unmodeled dynamics. Subsequently, Section VI reports the experimental results on different systems. Finally, the conclusions are given in Section VII.

II. PRELIMINARIES

Jerk-limited trajectories with good continuity are desirable for applications requiring smoothness, safety, and precision. Recently, the time-shifted cosine jerk trajectory has emerged as a promising solution. As shown in Fig. 2, a standard point-to-point trajectory is composed of an acceleration phase $[t_0, t_3]$, a cruise phase $[t_3, t_4]$, and a deceleration phase $[t_4, t_7]$. The

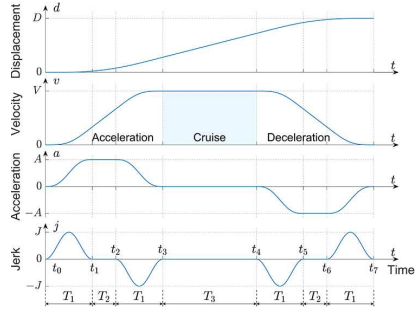


Fig. 2. Schematic of the standard cosine jerk profile.

acceleration and deceleration phases can be further divided into three segments: two cosine jerk segments and one constant acceleration segment. A , V , and D are the peak acceleration, peak velocity, and target displacement, respectively. The durations for cosine jerk, constant acceleration, and cruise segments are denoted by T_1 , T_2 , and T_3 , respectively. The cosine jerk segments ensure that the acceleration ramps up and down smoothly, allowing for a continuous snap (jerk derivative) profile. Consequently, the resulting trajectory exhibits high insensitivity to parameter uncertainties [20].

Let $j(t)$ denote the jerk profile, and the trajectory is defined as

$$j(t) = \begin{cases} \frac{J}{2}(1 - \cos(\frac{2\pi}{T_1}(t - t_i))), & t_0 \leq t \leq t_1, t_6 \leq t \leq t_7 \\ -\frac{J}{2}(1 - \cos(\frac{2\pi}{T_1}(t - t_i))), & t_2 \leq t \leq t_3, t_4 \leq t \leq t_5 \\ 0, & \text{otherwise} \end{cases} \quad (1)$$

where t_i denotes the start time of the corresponding segment, and $J = 2A/T_1$ is the peak value of jerk. This trajectory can be viewed as a superposition of the trapezoidal velocity profile by an embedded prefilter, which is described by the following transfer function:

$$H_{\cos}(s) = \frac{(1 - e^{-sT_1})}{T_1} \left[\frac{(2\pi/T_1)^2}{s(s^2 + (2\pi/T_1)^2)} \right]. \quad (2)$$

As illustrated in (2), $H_{\cos}(s)$ possesses three poles: one located at the origin and a pair at $\pm j2\pi/T_1$. The pole at the origin acts as an integrator, providing a low-pass filtering effect that effectively reduces vibrations resulting from unmodeled high-frequency dynamics. Additionally, $H_{\cos}(s)$ features an infinite sequence of equally spaced zeros along the imaginary axis. The first pair of zeros, located at $\pm j2\pi/T_1$, is neutralized by its own poles, while the remaining zeros can be utilized to counteract the system poles, which can be expressed as follows:

$$s_z = \pm j(k + 1)\frac{2\pi}{T_1}, \quad k = 1, 2, 3, \dots \quad (3)$$

The dynamic response of the system to base acceleration excitation during motion is primarily governed by its dominant mode, which can generally be represented as a second-order harmonic oscillator characterized by the transfer function $G_0(s) = \omega_n^2/(s^2 + 2\zeta\omega_n + \omega_n^2)$, where the natural frequency ω_n and the damping ratio ζ define the complex conjugate poles

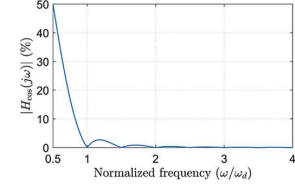


Fig. 3. Frequency response magnitude of the embedded $H_{\cos}(s)$.

of the system $s_p = \beta \pm j\omega_d$ with $\beta = -\zeta\omega_n$, $\omega_d = \omega_n\sqrt{1 - \zeta^2}$. Despite the complex dynamics of real systems, this simplified lumped parameter linear model captures the most fundamental vibration characteristics and reveals key physical principles and insights. In engineering practice, higher-order systems are often decomposed into combinations of second-order systems, while many mildly nonlinear systems can be effectively linearized about a specific operating point when constrained to small deviations. Moreover, as will be shown later, the inherent robustness of the proposed technique to parameter estimation errors and unmodeled dynamics allows it to remain effective even in the presence of certain system nonlinearities.

As indicated in previous studies [20], the residual vibration is most effectively minimized by placing the zeros of the prefilter in the closest achievable proximity to the poles of the system mode. Therefore, for optimal vibration reduction with minimal duration, the time period of the cosine jerk segment should be set to twice the vibration period T_d

$$T_1 = 2T_d = 4\pi/\omega_d. \quad (4)$$

Under this condition, the residual response nearly vanishes for lightly damped systems. In fact, when (4) is met, the frequency response magnitude of $H_{\cos}(s)$ expressed in (5) is zero at $\omega = \omega_d$, as shown in Fig. 3, and thus the trajectory does not contain any spectral component at the resonant frequency. Fig. 3 also reveals the high-frequency attenuation behavior, which mitigates the impact of unmodeled modes

$$\left| H_{\cos}(j\omega) \right| = \frac{8\pi^2}{T_1^3} \left| \frac{\sin(\omega T_1/2)}{\omega((2\pi/T_1)^2 - \omega^2)} \right|. \quad (5)$$

However, to the best of our knowledge, no prior work has addressed a complete solution for the cosine jerk trajectory under explicit frequency constraints. Moreover, its performance is compromised for highly damped modes, as damping causes the system poles to shift along the real axis. Therefore, tuning the time parameter of the above cosine jerk model alone is insufficient to completely eliminate the damped vibration mode unless its structure is modified, as will be detailed in the subsequent section.

III. ASYMMETRIC COSINE JERK TRAJECTORY FOR VIBRATION SUPPRESSION

A. Adaptation of $H_{\cos}(s)$ for Damping Effects

To fully compensate for the vibration mode of the system, the zeros of the input trajectory should be placed to coincide with the system poles. This can be achieved by performing a linear

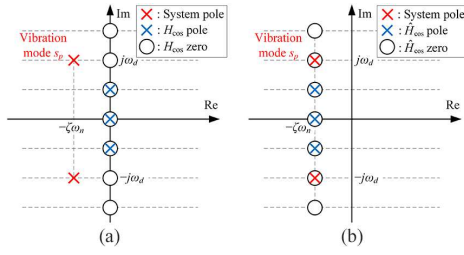


Fig. 4. Pole-zero cancellation for: (a) $H_{\cos}(s)$; and (b) $\hat{H}_{\cos}(s)$ with damping ($\zeta \neq 0$).

transformation in the complex domain such that the zeros of the trajectory shift by a desired distance β , as shown in Fig. 4.

The mapping in the complex domain for linear transformation is defined as

$$\hat{s} = s - \beta. \quad (6)$$

Applying this mapping to $H_{\cos}(s)$, we get a transfer function that inherently has zeros at $s_z = \beta \pm j\omega_d$

$$\hat{H}_{\cos}(s) = k_c H_{\cos}(s - \beta) \quad (7)$$

where k_c is a compensation coefficient for the unitary static gain, which ensures that the static gain satisfies the following rule after the mapping:

$$\lim_{s \rightarrow 0} \hat{H}_{\cos}(s) = 1 \Rightarrow \lim_{s \rightarrow 0} k_c H_{\cos}(s - \beta) = 1. \quad (8)$$

Consequently, by resolving the value of k from the above equation, the final transfer function for the modified cosine prefilter is obtained as

$$\hat{H}_{\cos}(s) = \frac{k_c}{T_1} \left[\frac{1}{(s - \beta)} - \frac{(s - \beta)}{(s - \beta)^2 + (2\pi/T_1)^2} \right] (1 - e^{-(s-\beta)T_1}) \quad (9)$$

where $k_c = -\beta T_1 (\beta^2 + ((2\pi/T_1)^2)/[((2\pi/T_1)^2)(1 - e^{\beta T_1})])$. The numbers of poles and zeros are the same as those of $H_{\cos}(s)$. By the inverse Laplace transform, the impulse response of $\hat{H}_{\cos}(s)$ is

$$h_{\cos}(t) = \begin{cases} \frac{k_c e^{\beta t}}{T_1} [1 - \cos(\frac{2\pi}{T_1} t)], & 0 < t < T_1 \\ 0, & \text{otherwise.} \end{cases} \quad (10)$$

Note that the vibration suppression condition (4) derived for the undamped system is not influenced by the mapping or compensation effect.

B. Asymmetric Damped Cosine Jerk Model

To reduce the time delay, this article proposes an asymmetric cosine jerk model for damped vibration mode cancellation, as shown in Fig. 5. Unlike a conventional symmetric S-curve, the peak kinematic values and time durations differ between acceleration and deceleration sections. Let T_{1a} and T_{2a} denote the time intervals of the cosine jerk and constant acceleration segments during acceleration, and T_{1d} and T_{2d} denote the corresponding intervals during deceleration. The total execution time

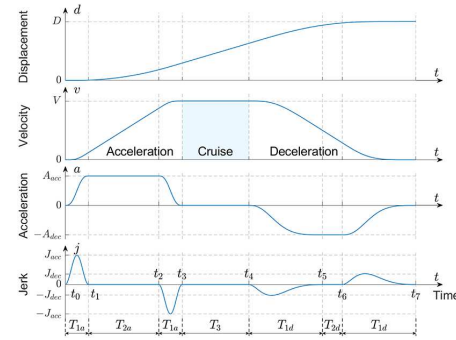


Fig. 5. Schematic of the proposed asymmetric cosine jerk profile (type 1). Since the velocity and acceleration bounds are reached, all seven segments are present.

is $T_{\text{tot}} = 2T_{1a} + 2T_{1d} + T_{2a} + T_{2d} + T_3$. Then the asymmetric cosine jerk profile can be expressed as

$$j(t) = \begin{cases} \frac{A_{\text{acc}}}{T_{1a}} [1 - \cos(\frac{2\pi}{T_{1a}}(t - t_0))], & t_0 \leq t \leq t_1 \\ -\frac{A_{\text{acc}}}{T_{1a}} [1 - \cos(\frac{2\pi}{T_{1a}}(t - t_2))], & t_2 \leq t \leq t_3 \\ -A_{\text{dec}} C_1 e^{\beta(t-t_4)} [1 - \cos(\frac{2\pi}{T_{1d}}(t - t_4))], & t_4 \leq t \leq t_5 \\ A_{\text{dec}} C_1 e^{\beta(t-t_6)} [1 - \cos(\frac{2\pi}{T_{1d}}(t - t_6))], & t_6 \leq t \leq t_7 \\ 0, & \text{otherwise} \end{cases} \quad (11)$$

where $C_1 = -\beta(\beta^2 + ((2\pi/T_{1d}))^2)/[((2\pi/T_{1d}))^2(1 - e^{\beta T_{1d}})]$; A_{acc} and A_{dec} are respectively the peak acceleration values reached at the end of the acceleration ramp-up in the acceleration and deceleration phases. The expressions for acceleration $a(t)$, velocity $v(t)$ and displacement $d(t)$ can be obtained by successively integrating $j(t)$. The peak velocity reached at the end of the acceleration ramp-down is represented by

$$V = v(t_3) = A_{\text{acc}}(T_{1a} + T_{2a}) = A_{\text{dec}}(T_{1d} + T_{2d}). \quad (12)$$

The displacements during the acceleration and deceleration phases can be calculated by

$$\Delta d_{\text{acc}} = V(2T_{1a} + T_{2a})/2 \quad (13)$$

$$\Delta d_{\text{dec}} = V(T_{1d} + T_{2d}) - \frac{1}{2}(1 + e^{\beta T_{1d}}) \frac{A_{\text{dec}} T_{1d}^2}{1 - e^{\beta T_{1d}}} - V C_2 - \frac{A_{\text{dec}} T_{1d} T_{2d}}{(1 - e^{\beta T_{1d}})} - \frac{1}{2} A_{\text{dec}} T_{2d}^2 \quad (14)$$

where $C_2 = (3\beta^2 + (2\pi/T_{1d})^2)/(\beta(\beta^2 + (2\pi/T_{1d})^2))$.

Compared with the traditional cosine jerk model, introducing asymmetry increases flexibility and enables a faster start by allowing a higher peak jerk value during acceleration, while the jerk value during deceleration is optimized for vibration suppression. This property is particularly appealing for vibration control of flexible systems with a relatively high damping ratio, as vibration induced during the acceleration phase can be sufficiently damped by the end of the motion. By selecting appropriate trajectory parameters, the residual vibration, as well as the total positioning time, can be minimized.

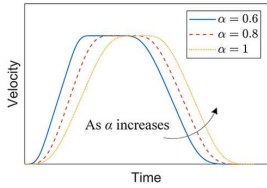


Fig. 6. Effects of the acceleration/deceleration ratio factor α on velocity profile of the asymmetric damped cosine jerk trajectory.

To fully define all kinematic features, it is essential to determine quantities T_{1a} , T_{2a} , T_3 , T_{1d} , T_{2d} , A_{acc} , and A_{dec} . These parameters are designed under the constraints of the desired displacement D and the actuator limitations, including the maximum velocity V_{\max} and the maximum acceleration A_{\max} . Without loss of generality, considering a positive displacement, the following constraint conditions should hold:

$$\begin{cases} d(t_7) = D \\ 0 \leq V \leq V_{\max}, 0 \leq A_{\text{acc}} \leq A_{\max}, 0 \leq A_{\text{dec}} \leq A_{\max} \\ T_{1a}, T_{2a}, T_3, T_{1d}, T_{2d} \geq 0. \end{cases} \quad (15)$$

It is necessary to determine the optimal parameters for vibration suppression while minimizing the trajectory execution time without violating the above constraints.

IV. PARAMETER TUNING

A. Acceleration Time Ratio

According to condition (4), the time period T_{1d} for the cosine jerk segments in the deceleration phase can be determined, i.e., $T_{1d} = 2T_d = 4\pi/\omega_d$. To achieve a minimum time trajectory, the maximum acceleration and velocity should be attained in the shortest time. However, depending on the target displacement and actuator limits, some trajectory segments may disappear.

To facilitate parameter tuning, we introduce an additional ratio factor α to modulate the time duration of the acceleration phase, which is defined as

$$\alpha = T_{\text{acc}}/T_{\text{dec}} \quad (16)$$

where $T_{\text{acc}} = 2T_{1a} + T_{2a}$ and $T_{\text{dec}} = 2T_{1d} + T_{2d}$ are the time durations for the acceleration and deceleration phases, respectively. The user can specify the value of α to adjust the trade-off between motion efficiency and vibration level. Fig. 6 provides an example of the evolution of the velocity profile for different values of α . A smaller value would lead to a shorter total motion duration, while a larger value leads to a slower but smoother start in acceleration. Moreover, the lower bound of α is constrained by the velocity and acceleration limits. The minimum allowable time for the acceleration phase is V/A_{\max} . Accordingly, the lower bound of α value is determined as

$$\alpha_{\min} = (V/A_{\max})/(2T_{1d} + T_{2d}). \quad (17)$$

Note that this value is related to the deceleration time determined by the constraint conditions. If an inappropriate value is selected for α by the user, this value needs to be adjusted to its

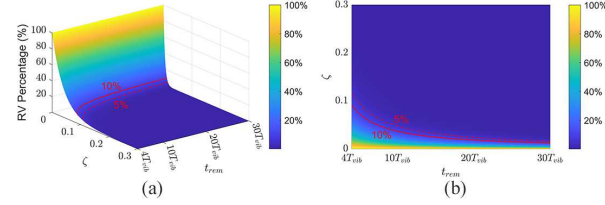


Fig. 7. Residual vibration (RV) percentage relative to Amp_{acc} for different damping ratios ζ and remaining times t_{rem} . (a) Surface plot. (b) Contour plot. The solid and dashed red lines indicate the contour lines for 10% and 5% RV, respectively.

lower bound value. To distinguish the selected initial value, we denote it as α_{ini} .

Since $T_{1d} = 2T_d$, the deceleration time is at least four times the vibration period. Assume that the amplitude of the motion-induced vibration response at the end of the acceleration phase is Amp_{acc} , and the remaining time from the end of the acceleration phase to motion completion is $t_{\text{rem}} = mT_d$ ($m \geq 4$). Then, the amplitude of the residual vibration envelope when the motion stops decays to

$$RV = \text{Amp}_{\text{acc}} e^{-\zeta \omega_n t_{\text{rem}}} |_{t_{\text{rem}}=mT_d} = \text{Amp}_{\text{acc}} e^{-2\pi m \zeta / \sqrt{1-\zeta^2}}. \quad (18)$$

Fig. 7 presents the surface and contour plots of the residual vibration percentage (relative to Amp_{acc}) versus ζ and t_{rem} . It shows that the vibration generated during the acceleration phase must attenuate to less than 10% of its initial value by the end of the motion if ζ is greater than 0.09, and to less than 5% if ζ is greater than 0.12. This indicates that effective vibration reduction can always be achieved when α is set close to its lower bound in cases of high damping, regardless of the constraint conditions. In addition, the value of m (the ratio of t_{rem} to T_d), determined by the moving distance, kinematic bounds, and modal properties, is a key factor when damping is insignificant. Therefore, for highly damped systems ($\zeta \geq 0.12$), α is preferably set closer to its lower bound to minimize motion duration. For lightly damped systems ($\zeta \leq 0.01$), since vibrations induced during the acceleration phase persist for an extended period, α can be set to 1 such that the vibration during acceleration is also eliminated. In this case, the trajectory becomes symmetric for undamped systems. For moderately damped systems ($0.01 < \zeta < 0.12$), α should be selected by comprehensively considering ζ , t_{rem} , and the required residual vibration bound according to Fig. 7. If additional constraints such as a jerk limit for smoother acceleration or a specific execution time are imposed, the value can be further fine-tuned.

B. Optimal Closed-Form Solution

We first determine the parameters for the deceleration phase. The acceleration time T_{acc} is inherently defined upon establishing the deceleration time T_{dec} . For each trajectory type, the acceleration phase has two possible scenarios depending on whether a constant acceleration segment is present. For simplicity of representation, the diagrams depict only cases with

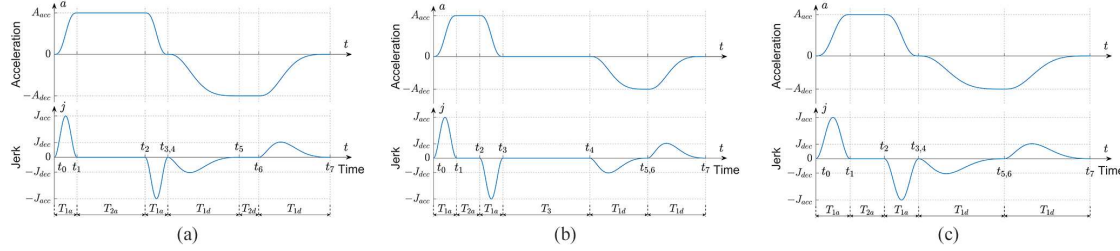


Fig. 8. Schematic of the proposed asymmetric cosine jerk profile. (a) Type 2: since the maximum allowable velocity and deceleration are unattainable, both the cruise and constant deceleration segments are absent. (b) Type 3: since the maximum allowable deceleration is unattainable, the constant deceleration segment is absent. (c) Type 4: since the maximum allowable velocity is unattainable, the cruise phase is absent.

a constant acceleration segment, and thus the trajectory is classified into four types. The detailed parameter design procedure is described below.

Combining (12) and (15), we can obtain

$$A_{dec} \leq V_{max}/T_{1d}, A_{dec} \leq A_{max}. \quad (19)$$

On the other side, the sum of the two displacements in the acceleration and deceleration phases should be no larger than the target displacement

$$\Delta d_{acc} + \Delta d_{dec} \leq D. \quad (20)$$

Since Δd_{acc} is influenced by α , we first verify condition (19). To ensure that A_{dec} satisfies (19), its value is selected as

$$A_{dec} = \min\{V_{max}/T_{1d}, A_{max}\}. \quad (21)$$

Depending on the value of A_{dec} , there are two cases.

Case 1: If $A_{dec} = V_{max}/T_{1d}$, A_{max} is unattainable because of the velocity limit during deceleration. Thus, $T_{2d} = 0$. Whether V_{max} is attainable depends on the constraint of the target displacement D . Assuming V_{max} is attainable, the minimum displacements during the acceleration and deceleration phases can be obtained from (13) and (14)

$$\Delta d_{acc1} = \Delta d_{acc}|_{T_{2d}=0, V=V_{max}} = \alpha V_{max} T_{1d} \quad (22)$$

$$\Delta d_{dec1} = \Delta d_{dec}|_{T_{2d}=0, V=V_{max}} = C_3 V_{max} T_{1d} - V_{max} C_2 \quad (23)$$

where $C_3 = (1 - 3e^{\beta T_{1d}})/(2(1 - e^{\beta T_{1d}}))$. Note that if V_{max} is reachable, the minimum allowable value for α is $V_{max}/(2A_{max}T_{1d})$ according to (17). Any value α_{ini} chosen by the user below this minimum should be adjusted to this minimum value. Then, we substitute (22) and (23) into (20) to verify the displacement constraint.

Based on whether condition (20) is satisfied, two subcases are distinguished here

Case 1-1: $\Delta d_{acc1} + \Delta d_{dec1} > D$

In this case, V_{max} is unattainable due to the target displacement, thus the constant velocity phase vanishes ($T_3 = 0$), as shown in Fig. 8(a). The actual peak velocity can be calculated as

$$V = D/(\alpha T_{1d} + C_3 T_{1d} - C_2). \quad (24)$$

Then the actual peak acceleration in the deceleration phase is recomputed by (12) as

$$A_{dec} = D/(\alpha T_{1d}^2 + C_3 T_{1d}^2 - C_2 T_{1d}). \quad (25)$$

If $\alpha = \alpha_{ini}$, (25) is the final solution; otherwise, it is necessary to check the minimum possible value of α . Substituting $\alpha = V/(2A_{max}T_{1d})$ into $\Delta d_{acc} + \Delta d_{dec}|_{T_{2d}=0} = D$ leads to

$$V = -C_3 A_{max} T_{1d} + C_2 A_{max} + \sqrt{(C_3 A_{max} T_{1d} - C_2 A_{max})^2 + 2A_{max} D}. \quad (26)$$

Subsequently, we calculate $\alpha_{min} = V/(2A_{max}T_{1d})$ from (26), and compare this value with α_{ini} . If $\alpha_{min} \geq \alpha_{ini}$, then (26) is the final solution and $A_{dec} = V/T_{1d}$. If $\alpha_{min} < \alpha_{ini}$, then α is set to α_{ini} , and the final solution is recalculated using (24) and (25).

Case 1-2: $\Delta d_{acc1} + \Delta d_{dec1} \leq D$

In this case, V_{max} is attainable ($V = V_{max}$), as depicted in Fig. 8(b). The constant velocity phase is required to achieve the desired displacement, of which the time period is calculated by

$$T_3 = (D - \alpha V_{max} T_{1d} - C_3 V_{max} T_{1d} + V_{max} C_2)/V_{max}. \quad (27)$$

Case 2: If $A_{dec} = A_{max}$, A_{max} is attainable during deceleration when disregarding the target displacement, whether V_{max} is attainable needs to be further discussed. When A_{dec} can reach A_{max} , the minimum displacements during the acceleration and deceleration phases are

$$\Delta d_{acc2} = \Delta d_{acc}|_{T_{2d}=0, A_{dec}=A_{max}} = \alpha A_{max} T_{1d}^2 \quad (28)$$

$$\Delta d_{dec2} = \Delta d_{dec}|_{T_{2d}=0, A_{dec}=A_{max}} = C_3 A_{max} T_{1d}^2 - A_{max} C_2 T_{1d}. \quad (29)$$

Note that if A_{dec} can reach A_{max} , V must be no smaller than $A_{max} T_{1d}$. Consequently, according to (17), the minimum allowable value for α is 1/2. Any unsuitable value should be adjusted. Similarly, we substitute (28) and (29) into (20) to verify the displacement constraint. Several potential subcases may arise here.

Case 2-1: $\Delta d_{acc2} + \Delta d_{dec2} > D$

In this situation, A_{max} is actually unattainable during deceleration due to the short displacement, and the same applies to V_{max} . Thus, $T_{2d} = 0$, $T_3 = 0$. This trajectory type is identical to that in *Case 1-1*. The minimum allowable value for α can be calculated from (26) using $\alpha_{min} = V/(2A_{max}T_{1d})$. If $\alpha_{min} \geq \alpha_{ini}$, then (26) is the final solution and $A_{dec} = V/T_{1d}$. If $\alpha_{min} < \alpha_{ini}$, then α is set to α_{ini} , and the final solution is calculated using (24) and (25).

Case 2-2: $\Delta d_{acc2} + \Delta d_{dec2} \leq D$

In this situation, A_{max} is attainable during deceleration ($A_{dec} = A_{max}$). Whether V_{max} is reachable necessitates further

evaluation according to the displacement constraint. Assuming V_{\max} is attainable, the minimum displacements during the acceleration and deceleration phases can be obtained as

$$\begin{aligned}\Delta d_{\text{acc}3} &= \Delta d_{\text{acc}}|_{V=V_{\max}} = \alpha V_{\max}(2T_{1d} + T_{2d})/2 \\ \Delta d_{\text{dec}3} &= \Delta d_{\text{dec}}|_{V=V_{\max}, A_{\text{dec}}=A_{\max}} = V_{\max}(T_{1d} + T_{2d}) - V_{\max}C_2 \\ &\quad - \frac{1}{2}(1+e^{\beta T_{1d}})\frac{A_{\max}T_{1d}^2}{1-e^{\beta T_{1d}}} - \frac{A_{\max}T_{1d}T_{2d}}{(1-e^{\beta T_{1d}})} - \frac{1}{2}A_{\max}T_{2d}^2\end{aligned}\quad (31)$$

where

$$T_{2d} = V_{\max}/A_{\max} - T_{1d}. \quad (32)$$

Note that if V_{\max} is reachable, the minimum allowable value for α is $V_{\max}/[A_{\max}(2T_{1d} + T_{2d})]$ according to (17). Any unsuitable value should be adjusted. Substituting (30) and (31) into (20) leads to two further possible subcases

Case 2-2-1: $\Delta d_{\text{acc}3} + \Delta d_{\text{dec}3} > D$.

Under this condition, V_{\max} is unattainable due to the short displacement, namely $T_3 = 0$, as illustrated in Fig. 8(c). The actual peak velocity is $V = A_{\max}(T_{1d} + T_{2d})$. By substituting this expression into the displacement constraint $\Delta d_{\text{acc}} + \Delta d_{\text{dec}}|_{A_{\text{dec}}=A_{\max}} = D$, we can solve for T_{2d} as follows:

$$T_{2d} = \frac{-C_5 + \sqrt{C_5^2 - 8(\alpha+1)[(\alpha+C_3)T_{1d}^2 - C_2T_{1d} - \frac{D}{A_{\max}}]}}{2(\alpha+1)} \quad (33)$$

where $C_5 = C_4T_{1d} - 2C_2$ and $C_4 = 3\alpha + 4 - 2/(1-e^{\beta T_{1d}})$. If $\alpha = \alpha_{\text{ini}}$, (33) is the final solution; otherwise, it is necessary to check the minimum possible value of α . Substituting $\alpha = (V/A_{\max})/(T_{1d} + (V/A_{\max}))$ into $\Delta d_{\text{acc}} + \Delta d_{\text{dec}}|_{A_{\text{dec}}=A_{\max}} = D$ leads to

$$\begin{aligned}V &= \left[C_2 + \frac{e^{\sigma T_{1d}} T_{1d}}{(1-e^{\sigma T_{1d}})} \right] \frac{A_{\max}}{2} \\ &\quad + \sqrt{\left[C_2 + \frac{e^{\sigma T_{1d}} T_{1d}}{(1-e^{\sigma T_{1d}})} \right]^2 \frac{A_{\max}^2}{4} + DA_{\max}}.\end{aligned}\quad (34)$$

Subsequently, we calculate $\alpha_{\min} = (V/A_{\max})/(T_{1d} + (V/A_{\max}))$ from (34), and compare this value with α_{ini} . If $\alpha_{\min} \geq \alpha_{\text{ini}}$, then (34) is the final solution and $T_{2d} = V/A_{\max} - T_{1d}$. If $\alpha_{\min} < \alpha_{\text{ini}}$, then α is set to α_{ini} , and the final solution is recalculated using (33)

Case 2-2-2: $\Delta d_{\text{acc}3} + \Delta d_{\text{dec}3} \leq D$.

Under this condition, V_{\max} is attainable ($V = V_{\max}$), and thus T_{2d} is obtained by (32). The trajectory contains all the segments, as shown in Fig. 5. The constant velocity phase is required to achieve the desired displacement, of which the time period is calculated as follows:

$$T_3 = (D - \Delta d_{\text{acc}3} - \Delta d_{\text{dec}3})/V_{\max}. \quad (35)$$

At this point, the above procedure fully determines the optimal parameters T_{1d} , T_{2d} , T_3 and A_{dec} under all potential scenarios. The total acceleration time is subsequently established as $T_{\text{acc}} = \alpha T_{\text{dec}}$. Note that for a given duration of the acceleration phase, there exists more than one solution for planning the

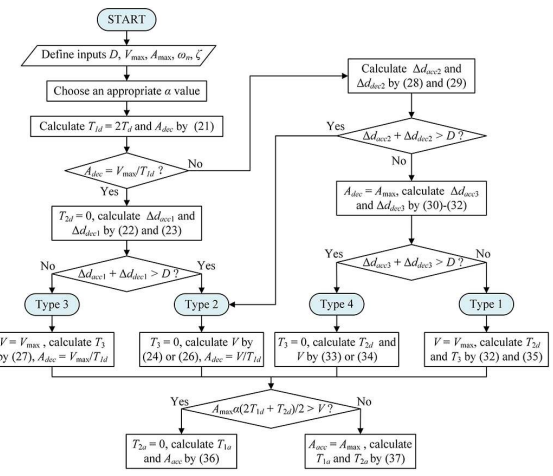


Fig. 9. Flowchart for trajectory parameter optimization.

acceleration profile. Here, we choose the solution that maximizes the duration of the cosine jerk segment to ensure optimal smoothness. The parameter derivation process for the acceleration phase contains two situations depending on whether A_{\max} is attainable during acceleration.

If $A_{\max}\alpha(2T_{1d} + T_{2d})/2 > V$, A_{acc} cannot reach A_{\max} , thus $T_{2a} = 0$. From (12), the other parameters are derived as

$$T_{1a} = \alpha(2T_{1d} + T_{2d})/2, \quad A_{\text{acc}} = 2V/(\alpha(2T_{1d} + T_{2d})). \quad (36)$$

Conversely, if $A_{\max}\alpha(2T_{1d} + T_{2d})/2 \leq V$, A_{\max} can be reached ($A_{\text{acc}} = A_{\max}$). The other parameters are derived as

$$T_{1a} = \alpha(2T_{1d} + T_{2d}) - \frac{V}{A_{\max}}, \quad T_{2a} = \frac{V}{A_{\max}} - T_{1a}. \quad (37)$$

In summary, to determine the optimal motion parameters, first select the value of α for a fast start. Then, identify the trajectory type and calculate the corresponding deceleration phase parameters, followed by the acceleration phase parameters. Fig. 9 presents the optimization flowchart. Note that in the special case where $\zeta = 0$, L'Hospital's rule should be applied to the derived formulas.

V. ROBUSTNESS ANALYSIS

A. Effects of Unmodeled System Dynamics

The proposed damped cosine trajectory with the embedded prefilter $\hat{H}_{\cos}(s)$ can fully eliminate vibrations if the system dynamics are accurately described by a second-order model. However, as mentioned earlier, most industrial machines possess additional dynamics that can influence performance. If the system model incorporates an extra stable dynamic component $G_a(s)$ in addition to the nominal model $G_0(s)$, the overall transfer function becomes $G(s) = G_0(s)G_a(s)$. Thus, due to linearity, the system response to a step input filtered by $\hat{H}_{\cos}(s)$, which corresponds to the acceleration evolution, is

$$Y(s) = G(s)\hat{H}_{\cos}(s)\frac{1}{s} = G_a(s) \left(G_0(s)\hat{H}_{\cos}(s)\frac{1}{s} \right). \quad (38)$$

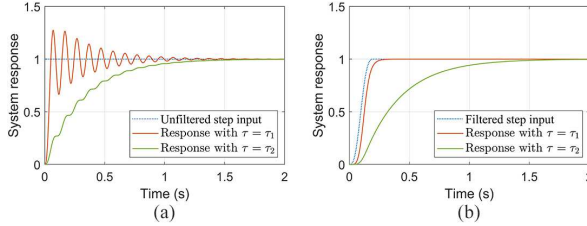


Fig. 10. System response of $G_0(s)$ with unmodeled dynamics $G_a(s) = 1/(\tau s + 1)$ for: (a) unfiltered unit step input; and (b) filtered unit step input, where $\omega_n = 2\pi \times 10 \text{ rad/s}$, $\zeta = 0.05$, with $\tau = \tau_1 = 1/(10\zeta\omega_n) = 0.0318 \text{ s}$ and $\tau = \tau_2 = 1/(\zeta\omega_n) = 0.318 \text{ s}$.

As a result, the actual response is simply the ideal response achieved with the nominal model $G_0(s)$ shaped by $G_a(s)$. Although $G_a(s)$ introduces additional modes into the response, it cannot excite the flexible mode of $G_0(s)$ that has been suppressed by $\hat{H}_{\cos}(s)$. Specifically, if $G_a(s)$ is completely damped, for instance, $G_a(s) = K/(\tau s + 1)$, where K and τ are the gain and time constant, respectively, the vibration suppression capability of the optimized trajectory remains unchanged regardless of the response speed of $G_a(s)$. Fig. 10 gives an example of the system response for the unfiltered and filtered unit step input with different time constants of $G_a(s)$. It shows that although the presence of the additional real pole leads to a longer response time to reach steady state compared with the nominal case, residual vibration is always entirely eliminated when $\hat{H}_{\cos}(s)$ is applied.

The prefilter $\hat{H}_{\cos}(s)$ is capable of effectively eliminating oscillations at integer multiples of the nominal damped natural frequency. Since the proposed technique targets only the dominant mode, it does not explicitly account for additional modes in multimode vibration systems. However, the poles of $\hat{H}_{\cos}(s)$ function as low-pass filters, substantially attenuating vibrations resulting from unmodeled high-frequency dynamics, as shown in the next section. $\hat{H}_{\cos}(s)$ possesses three poles, indicating a significant low-pass effect and smoothness in the optimized trajectory. The frequency response magnitude decays rapidly above the dominant mode frequency. A potential extreme situation arises when a mode exists in close proximity to the dominant mode. In such cases, the present approach can be combined with input shaping, each tailored to a specific mode to further enhance performance.

B. Simulation of Distributed Model

Distributed parameter models can more precisely describe actual flexible structures. Consider an upright thin cantilever beam with a rectangular cross section clamped to a horizontally moving base, as shown in Fig. 11(a). Let ρ , A , L , and EI denote the density, sectional area, length, and bending stiffness (consisting of Young's modulus E and moment of inertia I) of the beam, respectively. $w(z, t)$ is the transverse deflection of the beam relative to the base at position z and time t . Using Euler-Bernoulli theory, the dynamic behavior of the beam under base movement can be described by the following partial differential

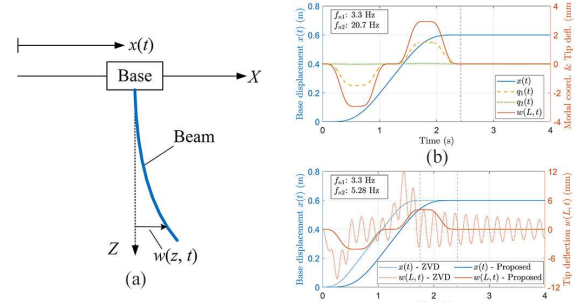


Fig. 11. (a) Schematic of an upright cantilever beam on a moving base. (b) Simulation results of the beam response with the proposed trajectory applied to the base. (c) Comparison of the beam response between the ZVD-shaped trapezoidal velocity trajectory and the proposed trajectory if f_{n2} shifts to $1.6f_{n1}$.

equation:

$$EI \frac{\partial^4 w(z, t)}{\partial z^4} + \rho A \frac{\partial^2 w(z, t)}{\partial t^2} = -\rho A \ddot{x}(t), z \in [0, L] \quad (39)$$

where $x(t)$ is the displacement of the base. Assuming the separability of spatial and temporal variables enables a closed-form solution for the bending deformation

$$w(z, t) = \sum_{i=1}^{\infty} \phi_i(z) q_i(t) \quad (40)$$

where $\phi_i(z)$ and $q_i(t)$ are the i th modal shape and generalized modal coordinate, respectively. The boundary conditions determining the natural frequencies and structural mode shapes are

$$w(0, t) = 0, \frac{\partial w(0, t)}{\partial z} = 0, \frac{\partial^2 w(L, t)}{\partial z^2} = 0, \frac{\partial^3 w(L, t)}{\partial z^3} = 0. \quad (41)$$

Setting $\ddot{x}(t) = 0$ in (39) yields the free vibration equation. Using separation of variables $w(z, t) = \phi(z)q(t)$, the spatial equation becomes $\phi'''(z) - \beta_i^4 \phi(z) = 0$, where $\beta_i^4 = \omega_n^2 \rho A / (EI)$. Applying (41) leads to

$$\phi_i(z) = \cosh(\beta_i z) - \cos(\beta_i z) - \frac{\cosh \lambda_i + \cos \lambda_i}{\sinh \lambda_i + \sin \lambda_i} [\sinh(\beta_i z) - \sin(\beta_i z)] \quad (42)$$

where $\lambda_i = \beta_i L$ is the positive root of the characteristic equation $1 + \cosh \lambda_i \cos \lambda_i = 0$. Using modal orthogonality and introducing damping, (39) transforms to the following modal ordinary differential equation:

$$\ddot{q}_i(t) + 2\zeta_i \omega_{ni} \dot{q}_i(t) + \omega_{ni}^2 q_i(t) = -\Gamma_i \ddot{x}(t) \quad (43)$$

where $\omega_{ni} = \beta_i^2 \sqrt{(EI/\rho A)}$, $\Gamma_i = \int_0^L \phi_i(z) dz / \int_0^L \phi_i^2(z) dz$, and ζ_i are the natural frequency, modal participation factor, and damping ratio of the i th mode, respectively.

Although (40) contains an infinite number of terms, only a few modes significantly contribute to the beam's bending in practice. If the first two modes are considered, and the beam parameters are assumed as: $\rho = 1240 \text{ kg/m}^3$, $A = 30 \text{ mm} \times 1 \text{ mm}$, $L = 0.25 \text{ m}$, $E = 2.02 \text{ GPa}$, $I = 2.5 \times 10^{-12} \text{ m}^4$, and $\zeta_i = 0.01$, then the modal frequencies are $f_{n1} = 3.3 \text{ Hz}$ and $f_{n2} = 20.7 \text{ Hz}$.

$= 20.7$ Hz. The proposed trajectory is optimized based on f_{n1} and is compliant with the following specifications: $D = 0.6$ m, $V_{\max} = 0.5$ m/s, $A_{\max} = 2$ m/s 2 , and $\alpha = 1$. Fig. 11(b) presents the simulation results with the trajectory applied to the base under zero initial conditions, including the reference position, modal coordinates, and tip deflection. The proposed trajectory does not excite either mode and yields nearly zero residual vibration. Additionally, the influence of the second mode is minimal for general uniform beams. Notably, we further consider a hypothetical extreme case where the second mode shifts closer to the first mode, i.e., $f_{n2} = 1.6 f_{n1} = 5.28$ Hz, while all other conditions remain unchanged. Fig. 11(c) illustrates the comparison results obtained from the ZVD-shaped trapezoidal velocity profile and the proposed trajectory. The ZVD-shaped trajectory successfully suppresses the first mode but excites the second mode and leads to significant residual vibration, whereas the proposed trajectory effectively eliminates residual vibration from both modes, even though only the first mode is considered in parameter tuning. This demonstrates that the proposed method is advantageous for complex systems characterized by numerous unmodeled dynamics.

VI. EXPERIMENTAL VALIDATION

A. Experiment 1: Medical Robot

1) *Experimental Setup:* To verify the effectiveness of the proposed method, experiments were performed on a KUKA LBR Med7 robotic platform, as shown in Fig. 12. The robot base is fixed to the floor to isolate vibrations not caused by motion. An endoscope is clamped with a custom-designed end-effector for manipulation. The endoscopic system guides robot-assisted intubation through airway visualization and requires vibration control to ensure safe, precise placement through the nostrils. The endoscope is characterized by a dominant mode with a natural frequency of 5.78 Hz and a damping ratio of 0.17. Nonlinear effects are present due to material properties and robot structure. The robot performs a linear transfer of the endoscope from the initial position to the target position near the nostrils of the human model. Different moving distances are tested to verify applicability. The end-effector coordinates of the initial points for the long and short distances are (0.6, -0.27, 0.67) m and (0.6, 0.16, 0.67) m, respectively, and the target point is (0.6, 0.28, 0.67) m, with the orientation fixed at $(\pi/2, \pi/5, \pi/2)$ rad in ZYX Euler angles. Table I lists the physical parameters used for trajectory generation. The settling bound can be specified according to the process requirements while considering equipment capabilities. A host computer running the Ubuntu operating system is used to control the robot. The proposed trajectory planning algorithm is implemented in Python IDLE on the computer, and the generated position data are then sent to the robot controller for tracking via the KUKA Sunrise Toolbox.

To capture the residual vibration response at the tip of the endoscope, a high-speed industrial camera MARS640-815UM from Vision Datum is mounted near the target position. This camera provides a resolution of 640 pixels \times 480 pixels with a frame rate of up to 815 frames per second (fps), enabling

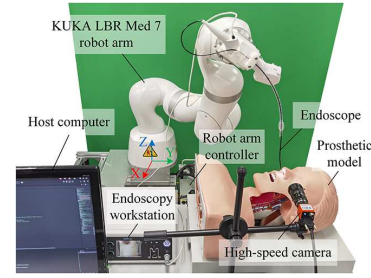


Fig. 12. Experimental setup.

TABLE I
EXPERIMENTAL PARAMETERS

| Parameter | Symbol | Value | Unit |
|----------------------|------------|--------------------------|----------|
| Moving distance | D | 0.55 (long)/0.12 (short) | m |
| Maximum velocity | V_{\max} | 0.6 | m/s |
| Maximum acceleration | A_{\max} | 2.2 | m/s 2 |
| Natural frequency | f_n | 5.78 | Hz |
| Damping ratio | ζ | 0.17 | |
| Settling bound | ϵ | ± 0.5 | mm |

accurate recording of the position evolution. A frame rate of 400 fps is used for experiments to avoid system parameter measurement errors resulting from dropped frames. The recorded videos are analyzed with the Tracker software to measure the displacement of the tip point. Data are retained from the first arrival of the endoscope tip at the desired position. The settling time is defined as the duration from motion start until the response settles within the specified range ϵ .

2) *Experimental Results:* The trapezoidal trajectory profile, the standard technique provided by the robot manufacturer, is taken as a reference baseline. Alternative methods for robust vibration suppression, including the well-known zero vibration and derivative (ZVD) input shaper [5], optimized fourth-order trajectory [3], damped sinusoidal trajectory [25], and asymmetric S-curve profile [29] are also tested for comparison. Here, α for the proposed trajectory is set to its lower bound to minimize the duration, as the damping is significant. To assess the robustness, we also performed experiments with trajectory parameters tuned with $\pm 20\%$ estimation errors in the modal frequency from its nominal value (4.62 and 6.94 Hz). In practice, the error typically remains within this range.

Fig. 13 compares the reference acceleration profiles from different techniques. The colored dashed vertical lines indicate motion completion times. Unlike the trapezoidal trajectory and ZVD shaper, which produce acceleration jumps that demand high servo bandwidth, the other trajectories ensure limited jerk. Fig. 14 illustrates the vibration displacements of the endoscope from different techniques for the long-distance motion in nominal and perturbed cases, along with the corresponding bar chart in Fig. 15. The blue region between the horizontal dashed lines represents the allowable error range ϵ . Table II summarizes the performance indices. The default trapezoidal velocity profile produces substantial peak residual vibration of nearly 4 mm, whereas the other optimized trajectories effectively reduce it

TABLE II
COMPARISON RESULTS OF DIFFERENT TRAJECTORIES IN EXPERIMENT 1

| Trajectory Model | Long Distance | | | | | | | | | Short Distance | | | | | | | | |
|--------------------------------------|-------------------------|------|------------|--------------------|-------|------------|-------------------|-------|------------|-------------------------|------|------------|--------------------|-------|------------|-------------------|-------|------------|
| | Residual Vibration (mm) | | | Execution Time (s) | | | Settling Time (s) | | | Residual Vibration (mm) | | | Execution Time (s) | | | Settling Time (s) | | |
| | -20% error | Nom. | +20% error | -20% error | Nom. | +20% error | -20% error | Nom. | +20% error | -20% error | Nom. | +20% error | -20% error | Nom. | +20% error | -20% error | Nom. | +20% error |
| Trapezoidal velocity | 3.83 | | | 1.189 | | | 1.617 | | | 3.15 | | | 0.473 | | | 0.902 | | |
| ZVD shaper [5] | 0.57 | 0.46 | 0.61 | 1.409 | 1.365 | 1.336 | 1.661 | 1.365 | 1.621 | 0.62 | 0.39 | 0.44 | 0.686 | 0.643 | 0.613 | 0.826 | 0.643 | 0.613 |
| Optimized 4 th -order [3] | 0.44 | 0.45 | 0.50 | 1.974 | 1.754 | 1.608 | 1.974 | 1.754 | 1.876 | 0.19 | 0.17 | 0.32 | 1.754 | 1.404 | 1.170 | 1.754 | 1.404 | 1.170 |
| Damped sinusoidal jerk [25] | N/A | 0.32 | 1.03 | N/A | 1.453 | 1.409 | N/A | 1.453 | 1.774 | N/A | N/A | N/A | N/A | N/A | N/A | N/A | N/A | N/A |
| Asymmetric S-curve [29] | 0.59 | 0.55 | 1.14 | 1.450 | 1.384 | 1.341 | 1.718 | 1.449 | 1.648 | N/A | N/A | N/A | N/A | N/A | N/A | N/A | N/A | N/A |
| Proposed | 0.28 | 0.22 | 0.53 | 1.522 | 1.428 | 1.366 | 1.522 | 1.428 | 1.468 | 0.13 | 0.27 | 0.40 | 0.994 | 0.840 | 0.741 | 0.994 | 0.840 | 0.741 |

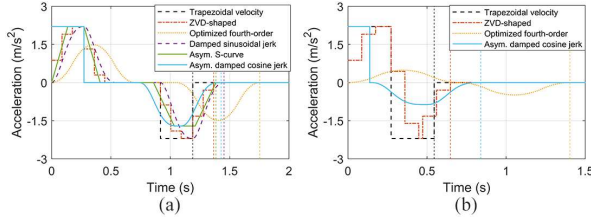


Fig. 13. Comparison of acceleration profiles in the nominal case for: (a) long-distance motion; and (b) short-distance motion.

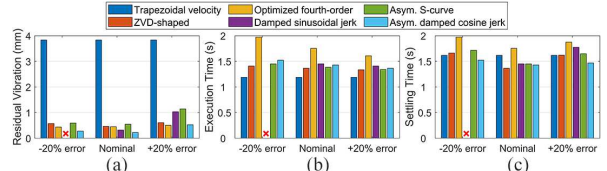


Fig. 15. Bar chart of results for different methods for long-distance motion. (a) Residual vibration. (b) Execution time. (c) Settling time.

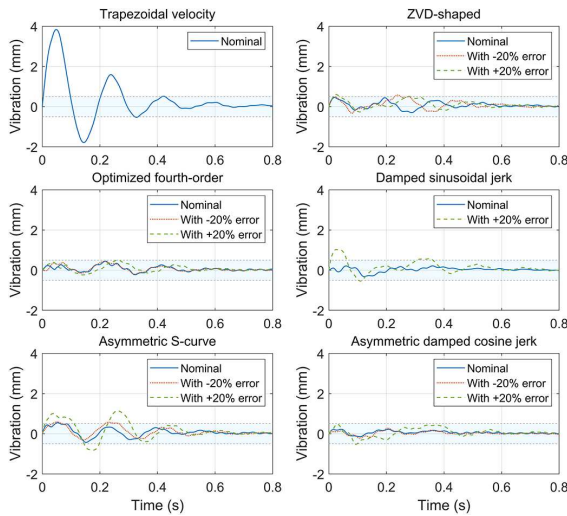


Fig. 14. Residual vibration responses of the endoscope with different techniques for long-distance motion.

in the nominal case, at the cost of a modest increase in duration. A small vibration inevitably remains in practice due to identification and tracking errors and nonlinearities, even with fine-tuning. Minor oscillations are visible in the vibration waveform, corresponding to the second mode at around 26 Hz. The asymmetric S-curve profile [29] yields slightly higher residual vibration than the others because damping is not compensated. Moreover, its asymmetry is not adjustable due to the coupling between the acceleration and deceleration segments. The proposed asymmetric damped cosine jerk profile yields the smallest residual vibration, providing a 94% reduction compared with the baseline due to strict zero-pole cancellation and excellent smoothness.

In the perturbed cases, most trajectories exhibit varying degrees of performance degradation, reflecting different robustness levels against system uncertainties. Smoothing to strengthen the low-pass characteristics or placing multiple zeros at the modal frequency can attenuate the harmonic content of the trajectory near the mode over a wider range. Therefore, smoother profiles tend to be more insensitive to parameter perturbations, while underestimating the modal frequency affects vibration less than overestimating it. The vibrations induced by the damped sinusoidal jerk and asymmetric S-curve trajectories increase appreciably under a + 20% error. Additionally, the former yields no valid solution for a - 20% error, as the tuned parameter does not meet the time optimality condition. The ZVD shaper yields relatively better results, but still slightly exceed the allowable error. Note that the shaper does not increase smoothness and thus cannot eliminate the effects of unmodeled dynamics. The proposed method shows enhanced insensitivity due to its highly smooth deceleration, with the vibration level undergoing only marginal changes and remaining nearly the lowest. The only exception is under a + 20% error, where it is slightly higher than that of the optimized fourth-order trajectory, since the latter possesses a zero of multiplicity four and has a much longer duration. Compared with the optimized fourth-order and damped sinusoidal jerk trajectories, the proposed profile shortens the duration by fully exploiting actuator capabilities during acceleration, thereby achieving the shortest settling time under perturbations.

Fig. 16 shows the results for the short-distance motion without a cruising phase. In this case, several existing techniques [25], [29] fail to produce a feasible solution, as they require all the kinematic bounds to be attainable. In contrast, the present method consistently yields feasible results, which is an important advantage. The resulting trajectory robustly attenuates the residual vibration in all cases, keeping it within the settling

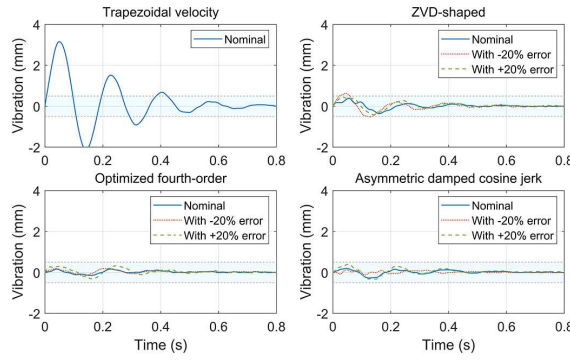


Fig. 16. Residual vibration responses of the endoscope with different techniques for short-distance motion.

bound. This confirms the analysis in Section IV that effective vibration reduction is always achievable under high damping regardless of constraint conditions. Additionally, the execution and settling times are shortened compared with the fourth-order trajectory. While the proposed trajectory reduces vibration more effectively than the ZVD shaper, it requires a longer duration since the deceleration phase lasts at least four times the vibration period. Selecting an appropriate technique based on actual operating conditions and requirements will maximize efficiency. Overall, the results clearly demonstrate the benefits of the method in damped vibration control under parameter uncertainties while minimizing trajectory duration.

B. Experiment 2: Linear Motion Stage

1) *Experimental Setup:* To validate the generality of the method on systems with different mechanical structures and dynamics, experiments were also conducted using a linear motion stage, as illustrated in Fig. 17. This system is commonly found in manufacturing settings, including automated assembly lines, semiconductor fabrication facilities, inspection instruments, and 3-D printers. The stage base is actuated by a linear motor (KFAC3002, SMARTWIN) in conjunction with a grating scale with $0.5 \mu\text{m}$ resolution mounted on the motor. To emulate the flexible behavior of the tool side, a polylactic acid (PLA)-based beam is integrated into the base. The beam features highly non-uniform properties with varying cross sections and attached local masses, highlighting the versatility of the technique in practical scenarios. While the response is dominated by the first mode at 7.41 Hz , it is also influenced by an unmodeled higher mode at 13.9 Hz . The damping ratio is quite low at approximately 0.01.

The motion stage is controlled by a host computer via a self-developed motion controller, which interfaces with a servo driver (CDHD, Servotronix) via EtherCAT. The trajectory optimization algorithms are executed on the host computer, generating trajectories that are sent to the controller as reference inputs. The velocity and current loop modes of the driver are configured for bus feedforward, and the controller transmits the planned position, velocity, and acceleration data every 1 ms to drive the motor. The constraints for stage motion are set as $D = 0.3 \text{ m}$, $V_{\max} = 0.6 \text{ m/s}$, $A_{\max} = 2 \text{ m/s}^2$, and $\epsilon =$

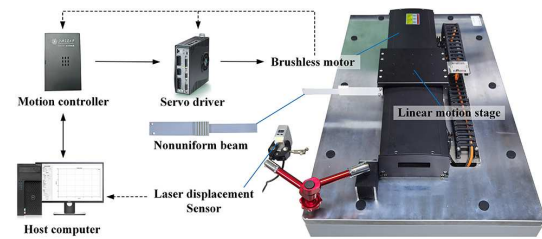


Fig. 17. Linear motion stage with a nonuniform flexible beam.

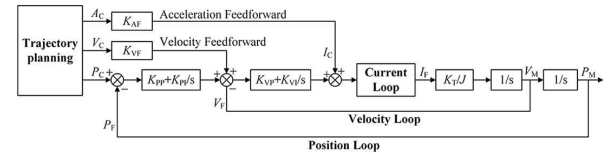


Fig. 18. Proposed PID + feedforward control architecture. A_C , V_C , P_C : acceleration, velocity, and position commands; K_{AF} , K_{VF} : acceleration and velocity feedforward coefficients; P_F , V_F , I_F : position, velocity, and current feedback; K_{PP} , K_{PI} , K_{VI} , K_{TI} : position loop proportional and integral gains; K_T : torque constant; J : moment of inertia; V_M , P_M : actual velocity and position.

$\pm 0.5 \text{ mm}$. The vibrations at the tip of the beam are monitored by a laser displacement sensor (FLR-50, FUWEI) with a sampling frequency of about 80 Hz.

2) *Control Structure Design and Tracking Performance:* Traditional three-loop proportional-integral-derivative (PID) control in motors is robust but suffers from phase lag, increased tracking errors, and a trade-off between speed and stability. Pure feedback cannot quickly compensate for dynamic changes, causing persistent errors. Thus, we introduce a feedforward compensation mechanism (see Fig. 18). Using the velocity and acceleration references generated by the trajectory planner, velocity, and acceleration feedforward terms are derived and injected directly into the velocity loop and current loop reference inputs, respectively, forming a combined feedforward-feedback control structure. Incorporating velocity feedforward increases the numerator order of the system transfer function, significantly enhancing the system's responsiveness to command signals and reducing tracking errors while maintaining stability and robustness. Fig. 19 presents the reference and actual position profiles recorded by the linear encoder. The results indicate that the proposed PID plus feedforward control reduces the maximum tracking error from 1.75 mm to $35 \mu\text{m}$ compared with traditional PID in the nominal case. The actual base movements closely match the designed reference profiles, demonstrating a high-performance servo system. Moreover, this holds true in both nominal and perturbed cases, indicating that the effect of modeling errors on tracking performance is negligible, and thus the vibration level depends primarily on the trajectory itself.

3) *Experimental Results:* Since the damping is light, α is set to 1 for the proposed trajectory, leading to a nearly symmetric profile. Similarly, the trapezoidal velocity trajectory is taken as

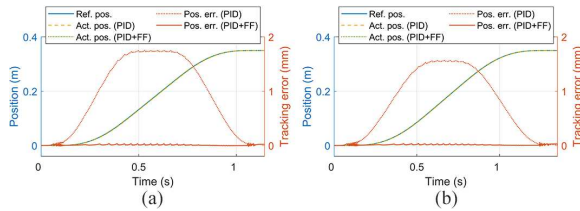


Fig. 19. Tracking performance comparison between traditional PID and the proposed PID + feedforward (FF) control for the proposed trajectory. (a) Nominal case. (b) Perturbed case.

TABLE III
COMPARISON RESULTS OF DIFFERENT TRAJECTORIES IN EXPERIMENT 2

| Trajectory Model | Residual Vibration (mm) | | Execution Time (s) | | Settling Time (s) | |
|--------------------------------------|-------------------------|-----------|--------------------|-----------|-------------------|-----------|
| | Nominal | Perturbed | Nominal | Perturbed | Nominal | Perturbed |
| Trapezoidal velocity | 12.8 | 4.24 | 0.980 | 1.014 | 4.014 | 4.269 |
| ZVD shaper [5] | 3.89 | 0.17 | 1.215 | 1.350 | 1.215 | 1.350 |
| Optimized 4 th -order [3] | 0.17 | 0.23 | 1.215 | 1.350 | 1.215 | 1.350 |
| Damped sinusoidal jerk [25] | 0.32 | N/A | 1.048 | N/A | 1.048 | N/A |
| Asymmetric S-curve [29] | 0.58 | 1.94 | 0.987 | 1.038 | 0.987 | 3.278 |
| Proposed | 0.23 | 0.22 | 1.144 | 1.350 | 1.144 | 1.350 |

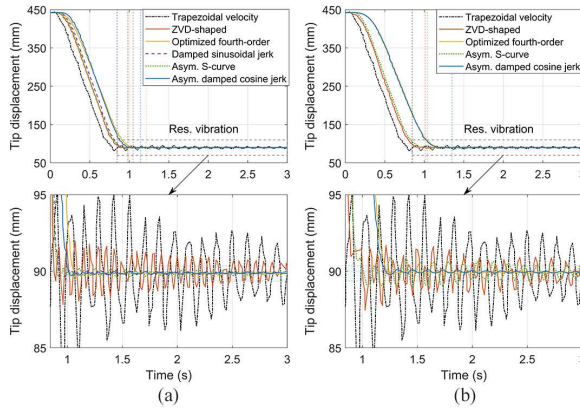


Fig. 20. Measured beam tip responses for different techniques. (a) Nominal case. (b) Perturbed case.

a baseline. A perturbed case with a -20% modal frequency estimation error is also tested for the other optimized trajectories. The measured beam tip displacements for different methods are presented in Fig. 20, and the results in terms of peak-to-peak residual vibration, execution time and settling time are reported in Table III. The trapezoidal trajectory excites both modes, producing large residual vibration of more than 12 mm. The ZVD-shaped trajectory effectively attenuates the first mode, but still induces pronounced vibration arising from the unmodeled second mode, and thus a long settling time. Smooth trajectories with limited jerk possess unique low-pass characteristics for mitigating the effects of unmodeled high-frequency dynamics. The asymmetric S-curve profile degrades significantly in the perturbed case, because its asymmetry is not adjustable, and therefore it cannot ensure that the vibration induced during acceleration is adequately damped. The other trajectories with continuous jerk achieve good performance in both nominal and perturbed cases, except that the damped sinusoidal jerk trajectory becomes invalid in the perturbed case. Under light damping, the proposed method achieves comparable settling time performance to existing methods when modeling errors are not considered. However, it ensures superior trajectory smoothness and provides significant benefits in improving vibration suppression robustness against system uncertainties, including parameter estimation deviations and unmodeled dynamics in the high-frequency domain.

VII. CONCLUSION AND FUTURE WORK

In this article, a novel asymmetric trajectory optimization method is proposed to minimize residual vibration. Following the analysis of cosine jerk profile characteristics, a modified trajectory model is designed to incorporate asymmetry and satisfy the pole-zero cancellation principle, which provides adaptability to damped cases and enables faster acceleration. A complete closed-form solution for any given constraint conditions has been derived based on the introduced ratio factor. By combining the potential to eliminate the dominant mode with the smoothness that mitigates the impact of neglected or varying modes, the optimized trajectory effectively attenuates vibration with improved robustness to modeling errors while minimizing time delay. Through comparative simulations and experiments on different systems, the effectiveness is demonstrated. This approach provides a practical route for precise positioning in general machines, offering low computational complexity and easy implementation without requiring any hardware modifications.

Strongly nonlinear systems whose vibration characteristics change significantly with configuration are more challenging to control without inducing residual vibrations. Future research will address large-scale modal variations and external disturbances during movement that affect performance. This can be achieved by independently tuning the duration of each cosine jerk segment in the trajectory based on time-dependent modal properties, or by integrating feedback strategies using additional sensor data into the control architecture to enhance adaptability. Furthermore, the method will be tested on more complex systems with multiple flexible components.

REFERENCES

- [1] Y. Ueno and H. Tachiya, "Suppressing residual vibration caused in objects carried by robots using a heuristic algorithm," *Precis. Eng.*, vol. 80, pp. 1–9, Mar. 2023.
- [2] A. Dumanli and B. Sencer, "Robust trajectory generation for multiaxis vibration avoidance," *IEEE/ASME Trans. Mechatron.*, vol. 25, no. 6, pp. 2938–2949, Dec. 2020.
- [3] D. Lee and C. W. Ha, "Optimization process for polynomial motion profiles to achieve fast movement with low vibration," *IEEE Trans. Control Syst. Technol.*, vol. 28, no. 5, pp. 1892–1901, Sep. 2020.
- [4] N. C. Singer and W. P. Seering, "Preshaping command inputs to reduce system vibration," *J. Dyn. Syst. Meas. Control. Trans. ASME*, vol. 112, no. 1, pp. 76–82, 1990.
- [5] H. Ghorbani, K. Alipour, B. Tarvirdizadeh, and A. Hadi, "Comparison of various input shaping methods in rest-to-rest motion of the end-effector of a rigid-flexible robotic system with large deformations capability," *Mech. Syst. Signal Process.*, vol. 118, pp. 584–602, Mar. 2019.

- [6] P. Boscaroli, D. Richiedei, and I. Tamellin, "Residual vibration suppression in uncertain systems: A robust structural modification approach to trajectory planning," *Robot. Comput. Integrat. Manuf.*, vol. 74, Apr. 2022, Art. no. 102282.
- [7] G. Hassan et al., "Time-optimal pick-and-throw s-curve trajectories for fast parallel robots," *IEEE/ASME Trans. Mechatron.*, vol. 27, no. 6, pp. 4707–4717, Dec. 2022.
- [8] L. Biagiotti, C. Melchiorri, and L. Moriello, "Optimal trajectories for vibration reduction based on exponential filters," *IEEE Trans. Control Syst. Technol.*, vol. 24, no. 2, pp. 609–622, Mar. 2016.
- [9] B. Nadir, O. Mohammed, N. Minh-Tuan, and S. Abderrezak, "Optimal trajectory generation method to find a smooth robot joint trajectory based on multiquadric radial basis functions," *Int. J. Adv. Manuf. Technol.*, vol. 120, no. 1–2, pp. 297–312, May 2022.
- [10] R. A. Rojas and R. Vidoni, "Designing fast and smooth trajectories in collaborative workstations," *IEEE Robot. Autom. Lett.*, vol. 6, no. 2, pp. 1700–1706, Apr. 2021.
- [11] L. Biagiotti and C. Melchiorri, "Optimization of generalized S-curve trajectories for residual vibration suppression and compliance with kinematic bounds," *IEEE/ASME Trans. Mechatron.*, vol. 26, no. 5, pp. 2724–2734, Oct. 2021.
- [12] F. Rauscher and O. Sawodny, "Efficient online trajectory planning for integrator chain dynamics using polynomial elimination," *IEEE Robot. Autom. Lett.*, vol. 6, no. 3, pp. 5183–5190, Jul. 2021.
- [13] Y. Fang, C. Gu, Y. Zhao, W. Wang, and X. Guan, "Smooth trajectory generation for industrial machines and robots based on high-order S-curve profiles," *Mech. Mach. Theory*, vol. 201, Oct. 2024, Art. no. 105747.
- [14] B. Ezair, T. Tassa, and Z. Shiller, "Planning high order trajectories with general initial and final conditions and asymmetric bounds," *Int. J. Rob. Res.*, vol. 33, no. 6, pp. 898–916, 2014.
- [15] R. Béarée, "New Damped-Jerk trajectory for vibration reduction," *Control Eng. Pract.*, vol. 28, no. 1, pp. 112–120, Jul. 2014.
- [16] Z. Chen, X. Gao, A. Wang, Z. Liang, and X. Zhang, "An online open-loop s-curve velocity profile control method for stepping motors on FPGA," *IEEE Trans. Ind. Electron.*, vol. 71, no. 12, pp. 16452–16462, Dec. 2024.
- [17] Y. Fang, J. Qi, J. Hu, W. Wang, and Y. Peng, "An approach for jerk-continuous trajectory generation of robotic manipulators with kinematical constraints," *Mech. Mach. Theory*, vol. 153, Nov. 2020, Art. no. 103957.
- [18] M. S. Halinga, H. J. Nyobuya, and N. Uchiyama, "Generation and experimental verification of time and energy optimal coverage motion for industrial machines using a modified S-curve trajectory," *Int. J. Adv. Manuf. Technol.*, vol. 125, no. 7–8, pp. 3593–3605, Apr. 2023.
- [19] H. Li, M. D. Le, Z. M. Gong, and W. Lin, "Motion profile design to reduce residual vibration of high-speed positioning stages," *IEEE/ASME Trans. Mechatron.*, vol. 14, no. 2, pp. 264–269, Apr. 2009.
- [20] C. W. Ha and D. Lee, "Analysis of embedded prefilters in motion profiles," *IEEE Trans. Ind. Electron.*, vol. 65, no. 2, pp. 1481–1489, Jul. 2017.
- [21] Y. Bai, X. Chen, H. Sun, and Z. Yang, "Time-optimal freeform s-curve profile under positioning error and robustness constraints," *IEEE/ASME Trans. Mechatron.*, vol. 23, no. 4, pp. 1993–2003, Aug. 2018.
- [22] C. J. Han, K. R. Song, and U. R. Rim, "An asymmetric S-curve trajectory planning based on an improved jerk profile," *Robotica*, vol. 42, no. 7, pp. 1–25, 2024.
- [23] P. Acharya, K. D. Nguyen, H. M. La, D. Liu, and I. M. Chen, "Nonprehensile manipulation: A trajectory-planning perspective," *IEEE/ASME Trans. Mechatron.*, vol. 26, no. 1, pp. 527–538, Feb. 2021.
- [24] T. Liu, J. Cui, Y. Li, S. Gao, M. Zhu, and L. Chen, "Time-optimal asymmetric S-curve trajectory planning of redundant manipulators under kinematic constraints," *Sensors*, vol. 23, no. 6, p. 3074, Mar. 2023.
- [25] L. Biagiotti, C. Melchiorri, and L. Moriello, "Damped harmonic smoother for trajectory planning and vibration suppression," *IEEE Trans. Control Syst. Technol.*, vol. 28, no. 2, pp. 626–634, Mar. 2020.
- [26] K. H. Rew and K. S. Kim, "A closed-form solution to asymmetric motion profile allowing acceleration manipulation," *IEEE Trans. Ind. Electron.*, vol. 57, no. 7, pp. 2499–2506, Jul. 2010.
- [27] D. M. Tsay and C. F. Lin, "Asymmetrical inputs for minimizing residual response," in *Proc. IEEE Int. Conf. Mechatron. (ICM)*, vol. 2005, 2005, pp. 235–240.
- [28] R. Sato and K. Shirase, "Analytical time constant design for jerk-limited acceleration profiles to minimize residual vibration after positioning operation in NC machine tools," *Precis. Eng.*, vol. 71, pp. 47–56, Sep. 2021.
- [29] C. W. Ha, K. H. Rew, and K. S. Kim, "Robust zero placement for motion control of lightly damped systems," *IEEE Trans. Ind. Electron.*, vol. 60, no. 9, pp. 3857–3864, Sep. 2013.
- [30] X. Li, X. Gao, J. Xiao, H. Cheng, Y. Zhang, and L. Hao, "Time-optimal general asymmetric S-curve profile with low residual vibration," *Mech. Syst. Signal Process.*, vol. 188, Apr. 2023, Art. no. 109978.